Research Article

Nanomedicine

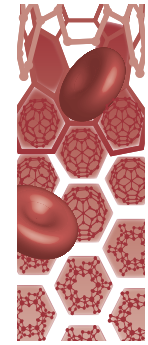

^{89}Zr-labelled anti-endoglin antibody-targeted gold nanoparticles for imaging cancer: implications for future cancer therapy

Aims: Antibody-labelled gold nanoparticles represent an attractive tool for cancer imaging and therapy. In this study, the anti-CD105 antibody was conjugated with gold nanoparticles (AuNPs) for the first time. The antibody biodistribution in mice before and after conjugation to AuNPs was studied, with a focus on tumor targeting. **Materials & methods:** Antibodies were radiolabelled with ^{89}Zr before conjugation to AuNPs (5 nm). Immunonanoconjugates were characterized *in vitro* in terms of size, stability in plasma and binding to the target. Quantitative PET imaging and ICP-MS analysis assessed *in vivo* distribution and specific tumor targeting of tracers. **Results:** The tumor uptake of immunoconjugates was preserved up to 24 h after injection, with high tumor contrast and selective tumor targeting. No major tracer accumulation was observed over time in nonspecific organs. ICP-MS analysis confirmed the antibody specificity after nanoparticle conjugation. **Conclusion:** The anti-CD105 antibody conjugation to AuNPs did not greatly affect CD105-dependent tumor uptake and the efficacy of tumor targeting for cancer detection.

Original submitted 29 April 2013; Revised submitted 20 September 2013

Keywords: ^{89}Zr • anti-endoglin antibody-targeted gold nanoparticles • biodistribution • cancer • CD105 • immuno-PET • molecular imaging

Linda Karmani, Virginie Bouchat, Caroline Bouzin, Philippe Levêque, Daniel Labar, Anne Bol, Gladys Deumer, Riccardo Marega, Davide Bonifazi, Vincent Haufroid, Carine Michiels, Vincent Grégoire, Olivier Feron, Stéphane Lucas, Thierry Vander Borght & Bernard Gallez*

*Author for correspondence:
Tel.: +32 2 7647391
Fax: +32 2 7647390
Bernard.Gallez@uclouvain.be
For full affiliations list, please see last page

Immunotargeted gold nanomaterials represent an attractive tool for cancer imaging and treatment [1]. During the past decade, the biomedical use of gold nanoparticles (AuNPs) has piqued in interest owing to their good biocompatibility and their interesting optical properties, which can be used to improve the management of cancer [2]. Recently, promising applications of AuNP-based systems as contrast agents for cancer imaging [3] or therapeutic agents for photothermal therapy have been reported [4]. Interestingly, AuNPs can be easily modified with various ligands, including specific monoclonal antibodies (mAbs). Functionalization of AuNP surfaces with mAbs enables them to have an adequate biodistribution as well as specifically target and be accumulated in cells that express or overexpress a specific surface membrane antigen. Thus, the resulting gold immunonanoconjugates are expected to be a good strategy for enhancing the efficacy of tumor targeting while reducing toxicity in normal tissues [5].

In this study, we functionalized AuNPs by choosing mAbs directed against endoglin (CD105), a homodimeric cell surface glycoprotein that is overexpressed on angiogenic vascular endothelial cells [6–13] and in some cancer cells, such as melanoma [14,15] and choriocarcinoma cells [16]. Furthermore, the vascular density of CD105, determined using anti-CD105 mAbs, is correlated with tumor prognosis [17], the risk of developing metastatic disease [18] and the recurrence of malignancy [19]. Recently, several studies have indicated that CD105 represents a more specific and sensitive marker for tumor angiogenesis and tumor progression than the commonly used pan-endothelial markers, such as CD34 and CD31, in various types of human malignancies [17,20–22]. Thus, CD105 targeting has been used as an antiangiogenic therapy based on attacking both the tumor

Future Medicine part of fsg

neovasculature as well as cancer cells that overexpress CD105 [23]. Nevertheless, tumors may still become resistant to antiangiogenic therapy [24]. Preclinical studies indicate that combining these agents with conventional cytotoxic agents or radiation therapy results in an additive or even synergistic antitumor effect [25]. Other approaches are to provide immunoconjugates with either immunotoxins or radioantibodies, which are effective for suppression of tumor growth [26–31] and metastasis [32]. Although anti-endoglin mAbs are successfully used as intrinsic therapeutic agents, they can also be used as targeting agents. Within this context, antibody-targeted AuNPs may represent an interesting combined approach for improving the efficacy of the standard inhibitors of angiogenesis thanks to the photophysical properties of AuNPs.

The main goal of this work is to characterize the impact of nanoparticle conjugation reactions on the target recognition properties of anti-CD105 mAbs *in vitro* and *in vivo*. Recently, we described the synthesis and characterization of cetuximab-targeted AuNPs. We investigated the impact of nanoparticle conjugation on cetuximab biodistribution and tumor targeting through an *ex vivo* biodistribution study [33] and *in vivo* noninvasive PET imaging [34]. We demonstrated that the conjugation of cetuximab to AuNPs did not significantly affect EGFR-dependent tumor uptake in mice. The present study was designed to assess the *in vivo* distribution of anti-endoglin mAbs conjugated to AuNPs compared to that of unconjugated mAbs, and to explore the effect of nanoparticle conjugation on tumor targeting. To trace these immunoconjugates, anti-CD105 mAbs were radiolabelled in advance using zirconium-89 (^{89}Zr). ^{89}Zr has an ideal long physical half-life (78.41 h) for PET imaging [35] of intact mAbs, which require time (typically 2–4 days) to reach optimal biodistribution and tumor targeting [36].

Materials & methods

Production & characterization of ^{89}Zr-labelled anti-CD105 mAbs

^{89}Zr was produced and purified in-house, as previously described [34,37,38]. The rat anti-mouse CD105 mAb was produced from a hybridoma (clone MJ7/18), which was provided by the Developmental Studies Hybridoma Bank (Iowa University, IA, USA). ^{89}Zr-labelled anti-CD105 mAbs (^{89}Zr-Df-Bz-NCS-anti-CD105) was prepared according to a protocol described previously [39,40]. First, the antibody was purified by protein G-affinity chromatography and dialysis into phosphate-buffered saline (PBS; 140 mM NaCl, 6 mM Na_2HPO_4, 3 mM KCl, 1 mM KH_2PO_4, pH 7.2) followed by size-exclusion chromatography on a Superdex 200 column (GE Healthcare Life Sciences, Belgium) using a 20 mM TRIS-HCl buffer (pH 7.5) containing 0.15 M NaCl. Then, the purified mAbs were functionalized with the bifunctional chelating agent p-isothiocyanatobenzyl-desferrioxamine (Df-Bz-NCS; Macrocyclics, TX, USA), as previously described [34]. Finally, the functionalized antibody (Df-Bz-NCS-anti-CD105) was purified by size exclusion chromatography using a PD10 column (GE Healthcare Life Sciences, Belgium) and radiolabelled with the produced ^{89}Zr-oxalate (74–111 MBq).

The radiochemical yield and purity were determined by using instant thin-layer chromatography (ITLC) and 20 mM citric acid (pH 4.9–5.1) as the mobile phase. ITLC migration was followed by radio-TLC detection (Mini-Gita TLC scanner, Raytest, Germany), which showed that the radiolabelled antibody migrated with Rf < 0.1, whereas unbound ^{89}Zr migrated to the solvent front. In addition, the integrity of the antibody after radiolabelling was checked by 10% SDS-PAGE gel (under nonreducing conditions) followed by radio-TLC detection (Bioscan system 200 imaging scanner), or by gel scanning using Phosphor Imager (Fujifilm FLA-5100) analysis.

Synthesis & characterization of ^{89}Zr-labelled anti-CD105 mAbs conjugated to AuNPs

AuNPs were synthesized and coated with plasma-polymerized allylamine (PPAA) through a physical vapor deposition technique (PVD), as previously described by our group [41]. The coated nanoparticles (AuNPs-PPAA) were purified as previously reported [33]. Anti-CD105 mAbs were conjugated to AuNPs-PPAA using carbodiimide chemistry and purified as previously described in our latest works [33–34]. The efficiency of the conjugation reaction between AuNPs-PPAA and ^{89}Zr-labelled anti-CD105 mAbs was assessed using 10% SDS-PAGE gel (under nonreducing conditions), followed by a radio-TLC analysis.

Physicochemical characterizations of AuNPs-PPAA and the immunonanoconjugates were performed as previously detailed [33,34,41,42]. In brief, TEM (Philips Tecnai 10 transmission electron microscope) was carried out to assess the morphology and size distribution of AuNPs-PPAA. Differential centrifugal sedimentation (DCS; DC 24000 Disk Centrifuge; CPS Instruments, Inc., FL, USA) was performed to determine the size of ^{89}Zr-labelled mAbs conjugated to AuNPs (^{89}Zr-anti-CD105-AuNPs-PPAA) by measuring the time required for these immunonanoconjugates to traverse a sucrose density gradient created in a disk centrifuge. This method used calibrated AuNPs coated layer by layer with polyelectrolytes to estimate the size of the tracer [33].

Cell culture & cell surface ELISA

A mouse melanoma cell line (B16F10-luc) and embryonic endothelial progenitor cells (eEPC) were maintained in alpha minimum essential medium (MEM-alpha with glutamine, Gibco-Invitrogen, Belgium) supplemented with 10% heat-inactivated foetal bovine serum (FBS, Gibco-Invitrogen, Belgium), 1% streptomycin–penicillin (Gibco-Invitrogen, Belgium) and 1% MEM nonessential amino acids (Gibco-Invitrogen, Belgium), or in Dulbecco's modified Eagle's medium (DMEM glucose 4.5 g l^{-1} without pyruvate, Gibco-Invitrogen, Belgium), supplemented with 10% fetal bovine serum and 1% streptomycin–penicillin respectively.

B16F10-luc or eEPC cells (10^4 cells per well) were grown in 96-well plates (Thermo Fisher Scientific, Belgium) 24 h prior to the ELISA test. Cells were washed once with PBS for cell culture (Lonza, Belgium), then fixed for a 10-min strict with PBS-containing 4% paraformaldehyde. After one wash with PBS, wells were blocked with 5% non-fat dry milk in PBS for 1 h at room temperature. Cells were rinsed twice with PBS and once with PBS containing 1% BSA (1% BSA-PBS) for 5 min. Anti-CD105 mAbs and anti-CD105-AuNPs-PPAA were added to the cells at various concentrations for 1 h at room temperature. Wells were washed six times with 1% BSA-PBS. Then, goat anti-rat IgG conjugated to peroxidase (Jackson Immunoresearch Laboratories, Belgium) diluted in 1% BSA-PBS at 0.32 mg ml^{-1} was added for 30 min at room temperature. After three washing steps with 1% BSA-PBS, the enzyme activity was revealed by adding 100 µl of TMB substrate (Merck Chemicals, Belgium) to each well for 20 min in the dark. The reaction was stopped with 250 mM HCl and the cell binding was quantified spectrophotometrically at 450 nm.

In vitro stability of radioimmunoconjugates in plasma

The *in vitro* stability of both purified ^{89}Zr-Df-Bz-NCS-anti-CD105 and ^{89}Zr-anti-CD105-AuNPs-PPAA was studied in fresh mouse plasma by incubating the solution of radiolabelled mAbs (1:2 v/v dilution at a final concentration of 1.1 MBq ml^{-1}; sodium azide added at 0.02%) at 37°C with stirring. At different times after incubation (6, 24, 48 and 72 h), aliquots of plasma (10 µl) were analyzed using radio-ITLC.

Comparative biodistribution studies in mice using animal PET/CT imaging

For the biodistribution assessment using PET imaging, C57BL/6J male mice (22–26 g, 5–6 weeks old; Janvier, France) bearing melanoma xenografts were used. The mice were inoculated subcutaneously in the flanks with 1×10^6 B16F10-luc cells (one or two tumors per mouse). After approximately 10 days, the diameter of the tumors had reached 7.5–8.5 mm and the mice were ready for *in vivo* experiments. All animal experiments were conducted in accordance with national and university animal care regulations.

To compare the pharmacokinetic profiles of native radiolabelled mAbs and those conjugated to AuNPs, two groups of three to five mice were injected intravenously in the lateral tail vein with either freshly prepared ^{89}Zr-Df-Bz-NCS-anti-CD105 or with ^{89}Zr-anti-CD105-AuNPs-PPAA (2.9–4.1 MBq; total of 350–400 µg mAbs per mouse). In addition, to assess the *in vivo* specificity of anti-CD105 mAbs conjugated to AuNPs, a group of three B16 melanoma-bearing mice (blocking group, two tumors per mouse) was injected with an excess of unlabelled anti-CD105 mAbs (2 mg mAbs per mouse) 2 h before the injection of ^{89}Zr-anti-CD105-AuNPs-PPAA (3.6–4.1 MBq; total of 200 µg mAbs per mouse), as previously described [43]. The blocking group was compared with the group of mice who received only ^{89}Zr-anti-CD105-AuNPs-PPAA without a saturating dose.

Whole-body PET images were acquired using a dedicated small-animal PET scanner (MOSAIC; Philips Medical Systems, OH, USA) with an intrinsic spatial resolution of 2.5 mm (full width at half maximum) [44]. The PET scans were followed by whole-body acquisitions using a helical CT scanner (NanoSpect/CT, Bioscan Inc., DC, USA) for anatomical reference. The PET/CT acquisitions were performed at different times after tracer injection (3, 6, 24, 48 and 72 h). All imaging procedures were performed under anesthesia with 1.5% isoflurane (Abbott Laboratories, Belgium)/oxygen gas mixture (2 l min^{-1}). Mice were maintained in a prone position on a heated animal bed at 37°C (Minerve, France). The PET acquisition durations were adapted to compensate for decay and ensure significant statistics (above 10,000 total counts). The emission scans were followed by transmission scans using a 370 MBq ^{137}Cs source for attenuation correction. All PET scans were reconstructed with a fully 3D iterative algorithm (3D-RAMLA) in a $128 \times 128 \times 120$ matrix, with a voxel size of 1 mm^3. After PET acquisition, the animal remained anesthetized and was transferred on the same bed from the PET scanner to the CT scanner (spatial resolution: 48 µm; x-ray tube voltage: 55 kVp; x-ray tube current: 145 µA; number of projections: 180; exposure time: 1000 ms). The CT projections were reconstructed with a voxel size of $0.221 \times 0.221 \times 0.221$ mm^3.

Before the PET and CT images were fused, the PET images were normalized according to a PET calibration factor including the positron branching ratio, the

10.2217/NNM.13.185

physical decay to the time of injection, the acquisition duration and the injected dose. This normalization was used to parameterize images in terms of percentage of the injected dose per ml. Regions of interest (ROIs) were delineated on the PET/CT fused images. The 2D ROIs were drawn on consecutive transversal slices using PMOD software (PMOD™, version 3.3, PMOD Technologies Ltd, Zurich, Switzerland), as previously described [34]. The tracer uptakes were assessed in the liver, lungs and tumors. Moreover, we defined a ROI, called background region, which was representative of tissues with low nonspecific uptake. The same background volume was drawn in the pelvic region of all animals, far from hot spots (organs with high uptake). The background signal was used to assess the specific-to-nonspecific tissue uptake, and particularly to estimate the tumor contrast, which was also expressed as tumor-to-background ratio, and which was calculated as the mean activity in the tumor region divided by the mean activity obtained in the background region. Finally, we quantified the blood activity over time by drawing ROIs within the ventricular cavity of heart, based on anatomical CT images fused with PET images (see Supplementary Figure 1 online at http://www.future-medicine.com/doi/full/10.2217/NNM.13.185).

Quantification of gold in tumors by ICP-MS

To compare the gold (Au) distribution of free nanoparticles to that of conjugated mAbs, two groups of four B16 melanoma-bearing mice were injected intravenously in the lateral tail vein with either freshly prepared AuNP-PPAA (a total of 36 µg Au per mouse) or with ^{89}Zr-anti-CD105-AuNPs-PPAA (a total of 18 µg Au per mouse, corresponding to 100 µg mAbs per mouse). Moreover, to confirm the *in vivo* specificity of anti-CD105 mAbs conjugated to AuNPs, a group of four B16 melanoma-bearing mice (blocking group) was injected with an excess of unlabeled anti-CD105 mAbs (2 mg mAbs per mouse) 2 h before the injection of anti-CD105-AuNPs-PPAA (a total of 22 µg Au per mouse, corresponding to a total of 200 µg mAbs per mouse). The blocking group was compared with the group of mice that received only anti-CD105-AuNPs-PPAA without a saturating dose. After 6 h, the animals were sacrificed. The blood and tumors were collected, weighed, freeze-dried and processed for gold content determination. The samples were hydrolyzed using 4 ml of pure 65% nitric acid (Merck Chemicals, Belgium) in a water bath at 60°C until complete solubilization of tissues. The analytical determination of gold (^{197}Au) in the samples was performed by inductively coupled plasma mass spectrometry (ICP-MS, type Agilent 7500cx, Agilent Technologies, Germany). The homogenized samples were diluted 100-times in a basic diluent (2% butanol, 0.05% EDTA, 1% NH_4OH and 0.05% triton) containing iridium (^{193}Ir) as an internal standard. The Au content of the samples was quantified by plotting the calibration curve with known concentrations of an Au standard solution (Merck Chemicals, Belgium) used for the external calibration. The amount of Au detected in the tumors was expressed as a percentage of the injected dose and as a tumor-to-blood ratio.

Statistical analysis

Data calculations were performed with Prism software (Graph Pad™ Software Inc., version 5.02). The differences in tissue uptake of radioactivity between two groups were considered significant if the p-values from nonparametric two-tailed Mann–Whitney tests were ≤ 0.05 or ≤ 0.01. The differences in tissue uptake of radioactivity at different times were assessed by one-way analysis of variance and the Tukey *post-hoc* test. The differences in tissue uptake of Au between two groups were considered significant if the p-values from unpaired t-tests (two-tailed) were ≤ 0.05 or ≤ 0.01.

Results

Characterization of radioimmunoconjugates before & after nanoparticle conjugation

Df-Bz-NCS-anti-CD105 was radiolabelled with ^{89}Zr with a mean radiochemical yield of 49.7 ± 13.2% (n = 3), whereas the radiochemical purity immediately after purification was >95%. The resulting specific activity was 55.5 ± 14.3 MBq mg^{-1} of mAbs (n = 3). Electrophoresis of ^{89}Zr-labelled anti-CD105 mAbs under nonreducing conditions followed by radio-TLC and autoradiography showed a single band of 150 kDa corresponding to ^{89}Zr-Df-Bz-NCS-anti-CD105 and a single peak of radioactivity (see Supplementary Figure 2A online at http://www.future-medicine.com/doi/full/10.2217/NNM.13.185), which means that the antibody integrity was preserved after the labelling reaction. Electrophoresis of antibody-labelled AuNPs under nonreducing conditions followed by radio-TLC showed a lower migration of ^{89}Zr-anti-CD105-AuNPs-PPAA compared with that of ^{89}Zr-Df-Bz-NCS-anti-CD105 and two peaks of radioactivity corresponding to the positions of the two species on the gel (see Supplementary Figure 2B online at http://www.future-medicine.com/doi/full/10.2217/NNM.13.185). The percentage of radioactivity linked to the peak of ^{89}Zr-anti-CD105-AuNPs-PPAA expressed the coupling reaction yield, which was over 75%. The nanoparticle diameters observed by TEM imaging ranged from 3 to 10 nm (mean diameter: 4.8 ± 1.7 nm) [33]. The mean diameter of anti-CD105-

AuNPs-PPAA was determined by differential centrifugal sedimentation and was estimated at approximately 102.6 ± 4.0 nm (Figure 1). This technique gives an 'apparent diameter', which may be affected by the non-perfect spherical shape of analyzed particle and by the nanoparticle coating. The size of anti-CD105-AuNPs-PPAA was not available through TEM imaging because the contrast was dominated by AuNPs, so that the nanoparticle coating was not visible. Moreover, it is likely that the carbodiimide reaction produces to some extent polymerized mAbs, which would increase the 'apparent diameter' of the conjugates. Finally, the *in vitro* stability of radioimmunoconjugates in plasma showed that ^{89}Zr was slightly dissociated from the antibody over time. Starting from a solution without free ^{89}Zr (100% purity), the percentages of dissociation were lower by 5% after 6 h, 10% after 24 h, and 15% after 48 and 72 h for both radioimmunoconjugates.

In vitro assessment of CD105 targeting

A cell-based ELISA study investigated the relative binding affinity of anti-CD105 mAbs towards endoglin-overexpressing cells before and after antibody conjugation to AuNPs. For this purpose, we chose the B16F10-luc melanoma cell line, known for its CD105 overexpression (CD105$^+$) [14,15]. The eEPC cell line was selected as negative control cells that do not express CD105, based on qualitative immunohistochemistry results and *in vitro* quantitative ELISA tests (data not shown). Different concentrations of anti-CD105 mAbs and anti-CD105-AuNPs-PPAA were tested on both CD105$^+$ and CD105$^-$ cells (Figure 2). As expected, anti-CD105 mAbs bound to CD105$^+$ cells in a concentration-dependent way, but not to CD105$^-$ cells. Interestingly, anti-CD105-AuNPs-PPAA also bound to CD105$^+$ cells in a concentration-dependent manner, suggesting retention of the target recognition property after nanoparticle conjugation. The relative binding affinity of anti-CD105 mAbs before and after conjugation to AuNPs was quantified as a half-maximal effective concentration (EC_{50}). The EC_{50} value was reduced from 1 µg ml^{-1} (for anti-CD105 mAbs) to 5 µg ml^{-1} (for anti-CD105-AuNPs-PPAA). The relative binding affinity remains on the same range (less than 1 log) before and after antibody conjugation to AuNPs. This lower CD105 binding affinity of conjugated antibody

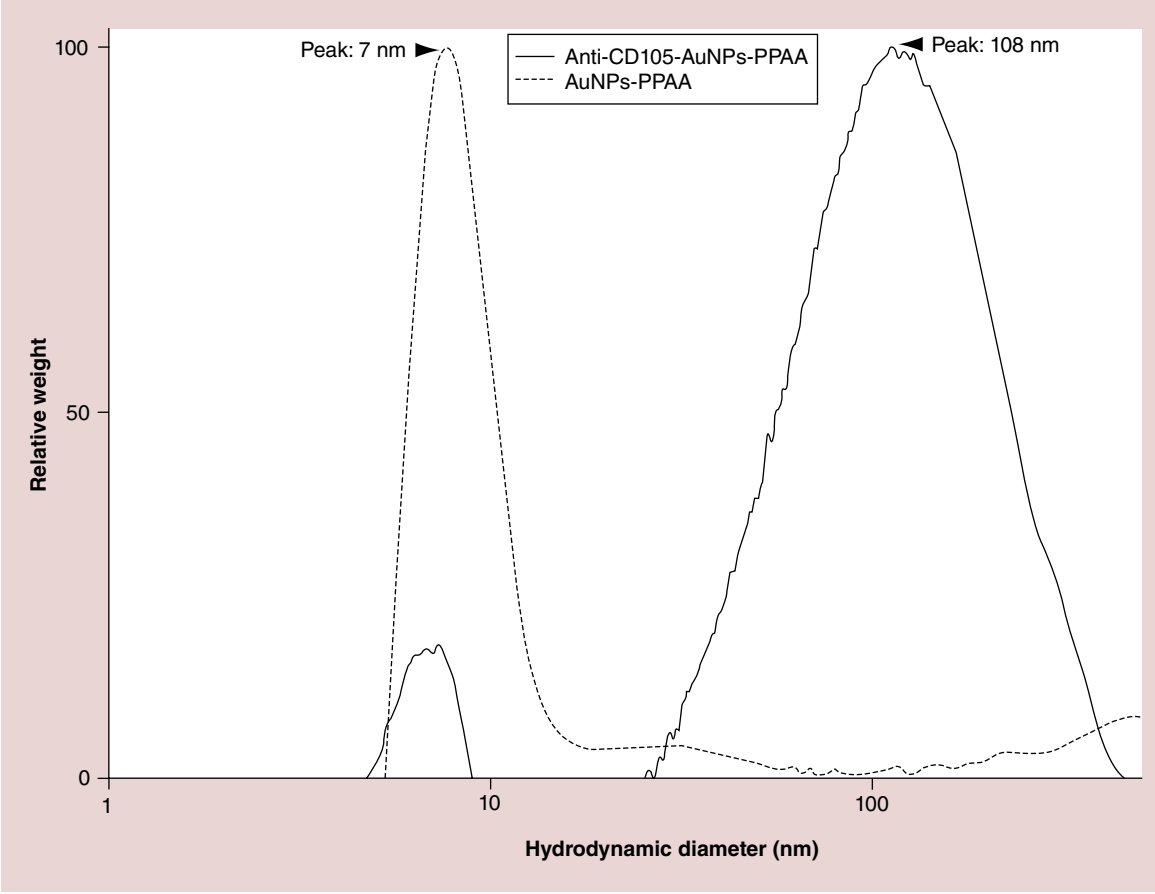

Figure 1. Size distributions given by differential centrifugal sedimentation for gold nanoparticles (dashed line) and anti-CD105-AuNPs-PPAA obtained after conjugation reaction (solid line).

10.2217/NNM.13.185

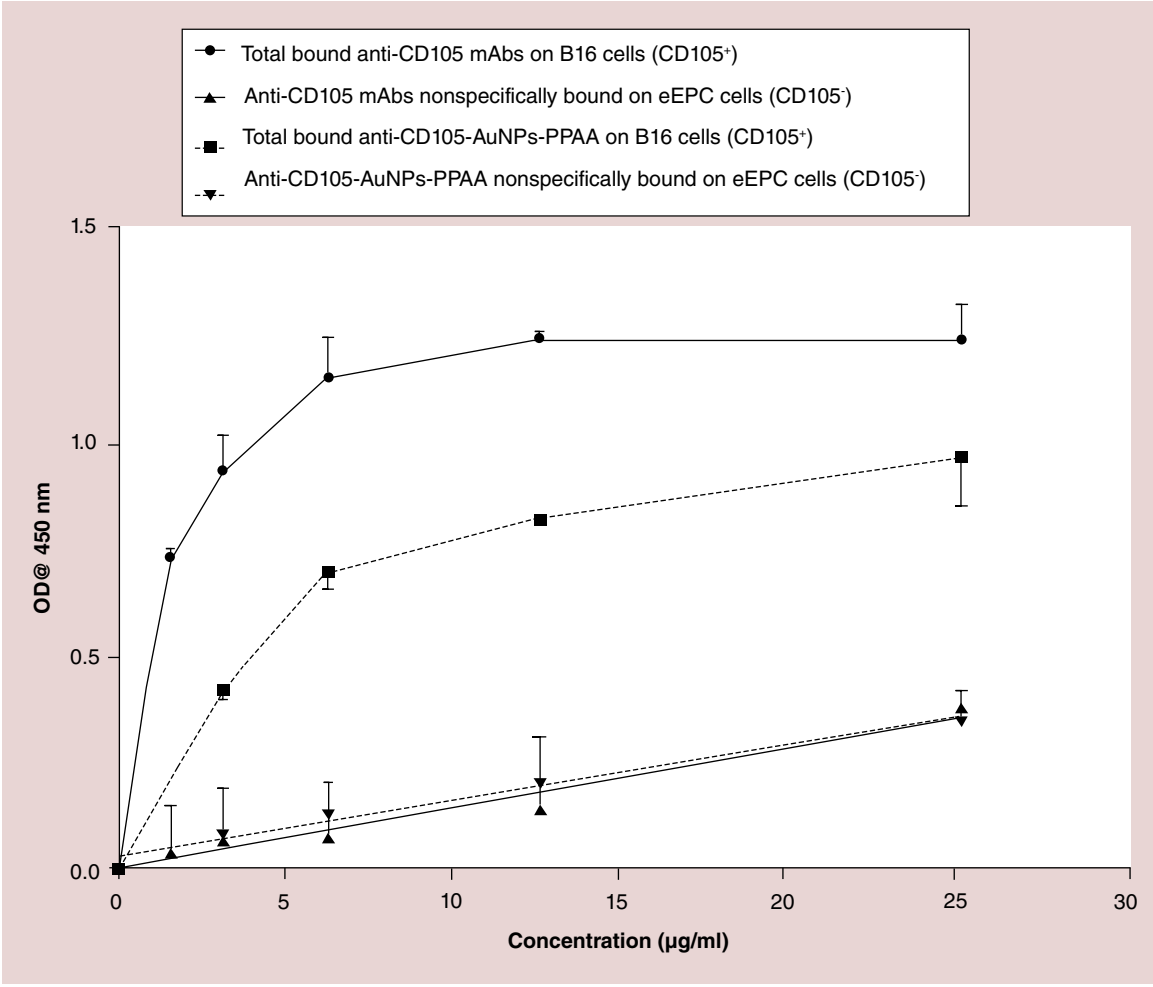

Figure 2. Surface ELISA for anti-CD105 monoclonal antibodies and anti-CD105-AuNPs-PPAA on CD105$^+$ (B16F10-luc) and CD105$^-$ (eEPC) cells. Different concentrations of mAbs and mAbs conjugated to AuNPs were tested. The concentration is expressed as µg of mAbs ml^{-1}. Results are presented as means ± SEM (n = 2–4).

was confirmed *in vivo* by blocking experiments as described below.

PET evaluation of ^{89}Zr-labelled anti-CD105 mAbs biodistribution in mice before & after coupling reaction to AuNPs

Two groups of B16 melanoma-bearing mice were injected with ^{89}Zr-Df-Bz-NCS-anti-CD105 or with ^{89}Zr-anti-CD105-AuNPs-PPAA, respectively. We then compared the pharmacokinetic behavior of ^{89}Zr-anti-CD105-AuNPs-PPAA with that of ^{89}Zr-Df-Bz-NCS-anti-CD105, as a reference compound. Figure 3 shows representative PET/CT images of mice bearing B16 tumor xenografts at different times after tracer injection (3, 6, 24, 48 and 72 h), and compares the distribution of ^{89}Zr-Df-Bz-NCS-anti-CD105 (Figure 3A) and ^{89}Zr-anti-CD105-AuNPs-PPAA (Figure 3B), respectively. At the different times after injection, accumulation of the two tracers was predominantly observed in the liver (red arrows) and in tumors implanted in the legs (yellow arrows). The lung uptake (green arrows) was observed only at early times (3 and 6 h). A similar pattern was observed for both radioimmunoconjugates, but with visually higher liver, spleen and lung uptakes for ^{89}Zr-anti-CD105-AuNPs-PPAA than for ^{89}Zr-Df-Bz-NCS-anti-CD105 (Figure 3). This distribution pattern remained constant at later times for the liver and spleen. 3D videos representing PET/CT fusion MIP (maximum intensity projection) of mice that received ^{89}Zr-Df-Bz-NCS-anti-CD105 or ^{89}Zr-anti-CD105-AuNPs-PPAA are available online as Supplementary Materials 3 & 4, respectively (see online at http://www.future-medicine.com/doi/full/10.2217/NNM.13.185).

For each time point considered, it must be mentioned that quantification of liver and lung uptakes showed no significant difference between the two groups (Figure 4), despite the visually more pronounced tracer uptake observed on PET/CT images for ^{89}Zr-anti-CD105-AuNPs-PPAA compared with

unconjugated antibody (Figure 3). The liver and lung uptakes were fast, with maximum values observed 3 h after tracer injection. The maximum liver uptake was approximately 14.9 ± 2.8%ID ml^{-1} for ^{89}Zr-anti-CD105-AuNPs-PPAA and 11.7 ± 1.1%ID ml^{-1} for ^{89}Zr-Df-Bz-NCS-anti-CD105 (Figure 4A), whereas the maximum lung uptake was approximately 15.2 ± 3.6%ID ml^{-1} for ^{89}Zr-anti-CD105-AuNPs-PPAA and 11.6 ± 1.0%ID ml^{-1} for ^{89}Zr-Df-Bz-NCS-anti-CD105) (Figure 4B).

The major differences between the biodistribution patterns were observed for tumor uptake (Figure 5). In the tumor, the kinetics were relatively fast for both conjugated and unconjugated mAbs (Figure 5A), with a maximum uptake reached after 24 h, followed by a plateau phase (6.5 ± 0.4%ID ml^{-1} for ^{89}Zr-Df-Bz-NCS-anti-CD105 and 4.6 ± 0.1%ID ml^{-1} for ^{89}Zr-anti-CD105-AuNPs-PPAA). A decrease in tumor uptake was observed starting 24 h after injection in favor of unconjugated mAbs. However, a continuous increase in tumor-to-background ratio was observed over time, with no difference between the two groups (Figure 5A). Finally, the specificity of tumor uptake was investigated by administering a saturating dose of unlabeled anti-CD105 mAbs 2 h before ^{89}Zr-anti-CD105-AuNPs-PPAA injection. This saturation experiment showed that the CD105 binding of ^{89}Zr-anti-CD105-AuNPs-PPAA was markedly reduced in the tumor up to 24 h after injection (Figure 6). In fact, the residual activity in the tumor was significantly lower for the blocking group at 3, 6 and 24 h after injection compared with the tumor uptake in mice injected with only ^{89}Zr-anti-CD105-AuNPs-PPAA. The tumor uptake value in the blocking group 6 h after injection (1.9 ± 0.2%ID ml^{-1}) was reduced by a factor of 2.5 compared with that for mice receiving only ^{89}Zr-anti-CD105-AuNPs-PPAA (4.7 ± 0.2%ID ml^{-1}).

Assessment of Au content in tumors by ICP-MS

Au content was measured in blood and tumors by ICP-MS at 6 h after tracer injection. In the normal situation, the presence of Au is detectable without background in the body. Figure 7A shows that the amount of Au expressed as a percentage of the injected dose in tumors was significantly higher for mice receiving anti-CD105-AuNPs-PPAA (3.3 ± 0.4%ID) than for those

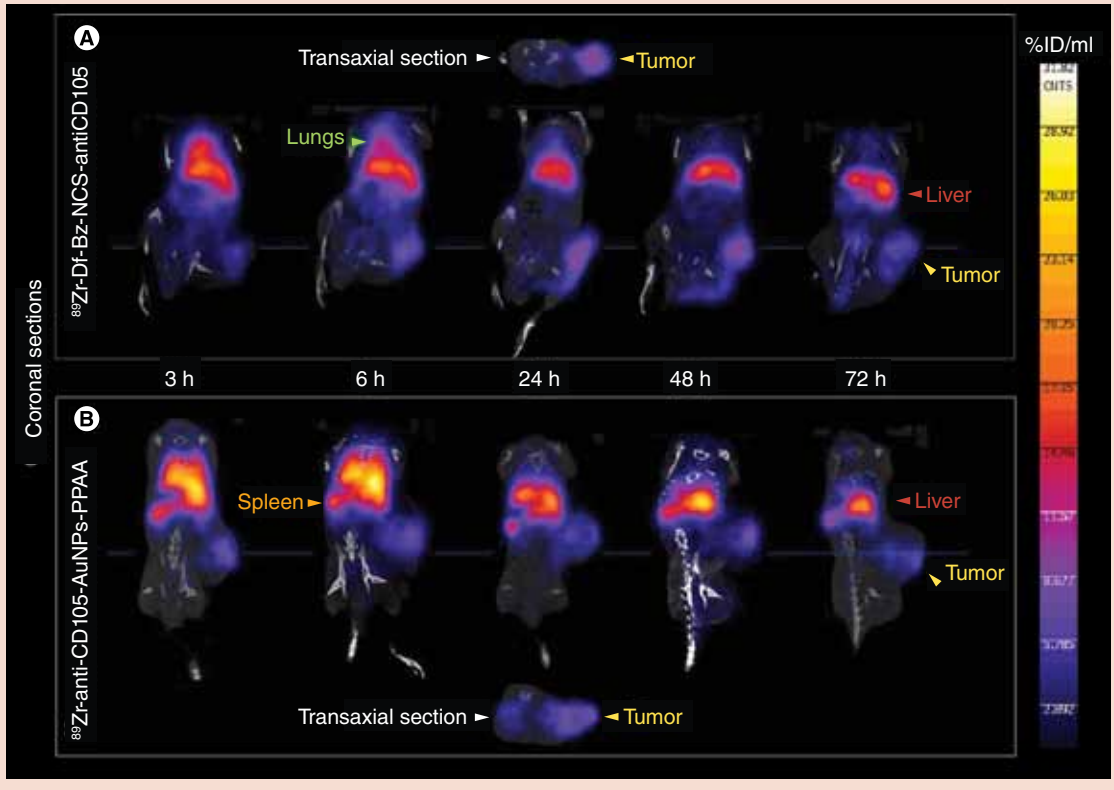

Figure 3. B16 melanoma-bearing C57BL/6J mice injected with (A) ^{89}Zr-Df-Bz-NCS-anti-CD105 or (B) ^{89}Zr-anti-CD105-AuNPs-PPAA (one tumor per mouse). PET/CT images were obtained at different times after injection (3, 6, 24, 48 and 72 h). Color scale, expressed as a percentage of the injected dose per ml (%ID ml^{-1}), indicated the radioactivity uptake levels in tumors (yellow arrows), in the liver (red arrows), in the spleen (orange arrows) and in the lungs (green arrows).

10.2217/NNM.13.185

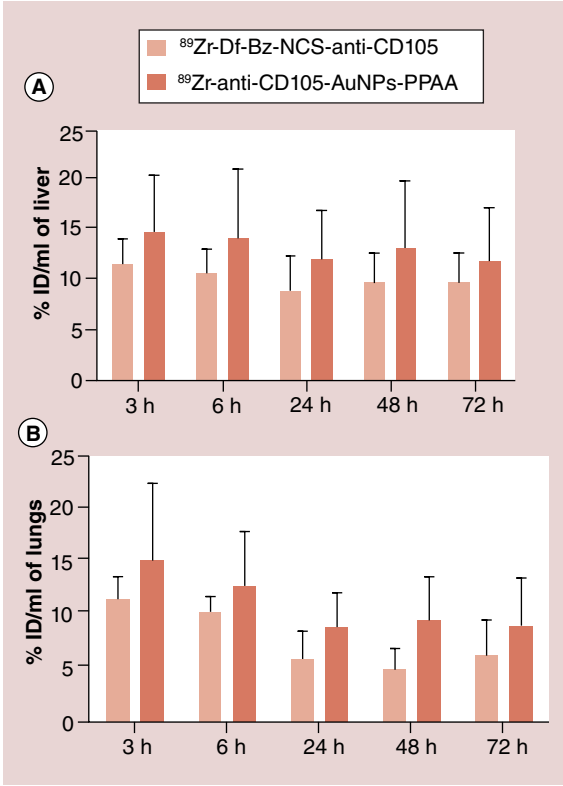

Figure 4. B16 melanoma-bearing C57BL/6J mice injected with ^{89}Zr-Df-Bz-NCS-anti-CD105 (light bars) or ^{89}Zr-anti-CD105-AuNPs-PPAA (dark bars). Injected activity ranged from 2.9 to 4.1 MBq, corresponding to a total of 350–400 µg mAbs per mouse. (A) Liver and (B) lung uptakes were quantified at 3, 6, 24, 48 and 72 h after injection. Results are expressed as means ± SD (n = 4–5 animals).

receiving AuNPs-PPAA (1.8 ± 0.1%ID). Moreover, the tumor-to-blood ratio was also significantly higher for the group of mice injected with anti-CD105-AuNPs-PPAA compared with the group of mice receiving free AuNPs (Figure 7B). The specificity of anti-CD105 mAbs after nanoparticle conjugation was confirmed by repeating the blocking experiment. The Au quantification in tumors after injecting a saturating dose of anti-CD105 mAbs 2 h before the anti-CD105-AuNPs-PPAA injection showed a significant decrease in Au content (1.3 ± 0.1%ID) compared with the group of mice receiving only anti-CD105-AuNPs-PPAA (3.3 ± 0.4%ID) at 6 h after injection (Figure 7A). The tumor-to-blood ratio values for the blocking group reached those for free nanoparticles and were significantly lower than those of mice receiving anti-CD105-AuNPs-PPAA without a prior saturating dose (Figure 7B).

Discussion

Because our group has recently developed a method for synthesizing AuNPs [41] and has successfully investigated the *in vivo* distribution of cetuximab conjugated to AuNPs [34], we have expanded our studies of nanoparticle vectorization through conjugation to mAbs by choosing the anti-CD105 mAb, which is still little-known but seems to be promising for targeting tumor cells and angiogenic vascular endothelial cells. We combined the targeting properties of anti-CD105 mAbs and the favorable imaging properties of ^{89}Zr. Our major goal was to further characterize the *in vivo* distribution of these antibody-targeted AuNPs, with a focus on tumor targeting, and to assess the *in vivo* impact of nanoparticle conjugation on the antibody target recognition by using noninvasive PET imaging.

The biodistribution pattern of ^{89}Zr-anti-CD105-AuNPs-PPAA and that of ^{89}Zr-Df-Bz-NCS-anti-CD105 showed liver, spleen and lung uptakes (Figure 3). First, the liver uptake quantification was not significantly different between the two groups (Figure 4A). It is known that one of the limitations of antibody-based imaging is the high background signal in the reticuloendothelial system (RES), which was particularly illustrated in our study by the liver uptake of the tracers. Furthermore, the large nanoparticles (100 nm) are not excreted in urine, which causes their extended presence in the circulation. Thus, the nanoparticles are eliminated from the blood by the RES and are accumulated in the spleen and liver [45]. On the other hand, the vascular endothelium structure of liver and spleen are discontinuous with large fenestrations, thus allowing nanomaterials (up to 100 nm) to pass through the endothelium and to be accumulated in these tissues [46]. Visually, the PET images showed that the liver uptake seemed to be increased after antibody conjugation to AuNPs (Figure 3). The colloidal properties of AuNPs could be the cause of this effect.

The same finding was observed for the lungs. Visually, the PET images showed that the lung uptake seemed to be higher for ^{89}Zr-anti-CD105-AuNPs-PPAA than for ^{89}Zr-Df-Bz-NCS-anti-CD105 only at early times (3 and 6 h after injection) (Figure 3). However, the lung uptake quantification showed no significant difference between the two groups at each time after injection (Figure 4B). First, no increase in lung accumulation was observed over time. The conjugates were cleared from lungs starting 24 h after injection. The alveolar macrophage activity of lungs might be the mechanism by which the conjugates were cleared [47]. The translocation of nanoparticles out of the lungs through lymphatic vessels was also described [48]. Further studies should be done to explore the lung clearance of our synthesized conjugates because the particle size, shape, surface properties and formulation affect the nanoparticle entrapment and the subsequent efficient uptake by macrophages [49]. Then, the constitutive expression of CD105 in vascularized organs like

lungs may explain the lung uptake. Moreover, previous studies showed that high levels of CD105 expression are seen in the distal vessels of mouse lung [50]. Other studies described the size-dependent biodistribution of AuNPs and showed that nanoparticles sized 100 nm were only significantly deposited in the liver, spleen and blood [51]. Finally, our blocking experiments showed the decrease of the immunanoconjugate's uptake in lungs, liver and spleen for mice receiving a saturating dose of unlabelled mAbs (data not shown). However, we cannot exclude some aggregation of the conjugates *in vivo* after intravenous injection, which might increase the lung uptake without any obvious respiratory problem observed, such as pulmonary embolism. In this regard, special attention should be paid if these nanoconjugates are injected at higher doses, such as for therapeutic purposes.

It must be mentioned that no major accumulation of radioactivity was observed in nonspecific organs, aside from the liver, spleen and lungs, and to a lesser extent bones. Starting 24 h after injection, PET images displayed distinct hot spots in the joints (shoulders and knees) that might be assigned to the detachment of ^{89}Zr from the desferal moiety (Figure 3). In fact, we observed that the two tracers were not fully stable under physiological conditions, with a release of up to 10% free ^{89}Zr being observed after 24 h of tracer incubation in plasma. Previous studies, including our latest study with cetuximab conjugated to AuNPs [34,52], reported a similar pattern of skeletal uptake and attributed the constant bone accumulation to the strong affinity of free ^{89}Zr ions for hydroxylapatite and phosphate constituents of bones. In fact, zirconium is known to bind to plasma proteins and it is later deposited in mineral bone [53]. Other studies hypothesized that high murine bone uptake is also due to the liver metabolism of the conjugate and the release of free ^{89}Zr into the circulation [54].

With regard to tumor targeting, we observed that the tumor uptake expressed as %ID ml^{-1} was significantly decreased after nanoparticle conjugation, starting 1 day after injection. This decrease was confirmed by the results of an *in vitro* ELISA test. Nevertheless, the tumor-to-background ratio remained good, without a significant difference before and after nanoparticle conjugation. Thus, the preservation of high tumor contrast after nanoparticle conjugation supports the good imaging properties of these radioimmunonanoconjugates.

We compared current data with those obtained previously with cetuximab conjugated to AuNPs [34]. For ^{89}Zr-cetuximab-AuNPs-PPAA, the tumor uptake was not significantly lower than for ^{89}Zr-Df-Bz-NCS-cetuximab up to 72 h after injection, with preserved tumor

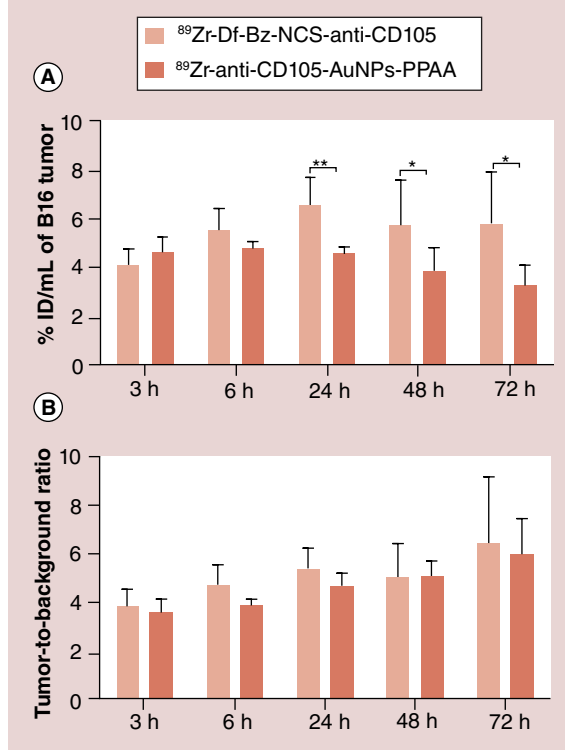

Figure 5. (A) Tumor uptake and (B) tumor-to-background ratio of ^{89}Zr-Df-Bz-NCS-anti-CD105 (light bars) or ^{89}Zr-anti-CD105-AuNPs-PPAA (dark bars) in B16 melanoma-bearing C57BL/6J mice at 3, 6, 24, 48 and 72 h after injection. Injected activity ranged from 2.9–4.1 MBq, corresponding to a total of 350–400 µg monoclonal antibodies per mouse. Results are expressed as means ± SD (n = 3–5 animals; 4–8 tumors). *p < 0.05; **p < 0.01.

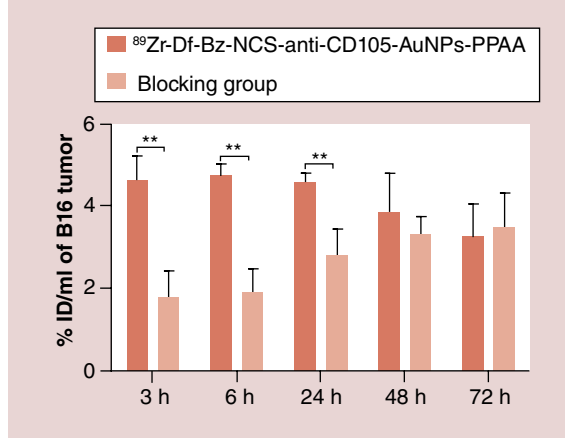

Figure 6. Tumor uptake of ^{89}Zr-anti-CD105-AuNPs-PPAA (2.9–4.1 MBq, a total of 350–400 µg monoclonal antibodies per mouse) or ^{89}Zr-anti-CD105-AuNPs-PPAA (3.6–4.1 MBq, a total of 200 µg monoclonal antibodies per mouse) after a blocking dose of unlabelled anti-CD105 monoclonal antibodies (2000 µg mAbs per mouse) in B16 melanoma-bearing C57BL/6J mice at 3, 6, 24, 48 and 72 h after injection. Results are expressed as means ± SD (n = 3 animals; 4–6 tumors). **p < 0.01.

10.2217/NNM.13.185

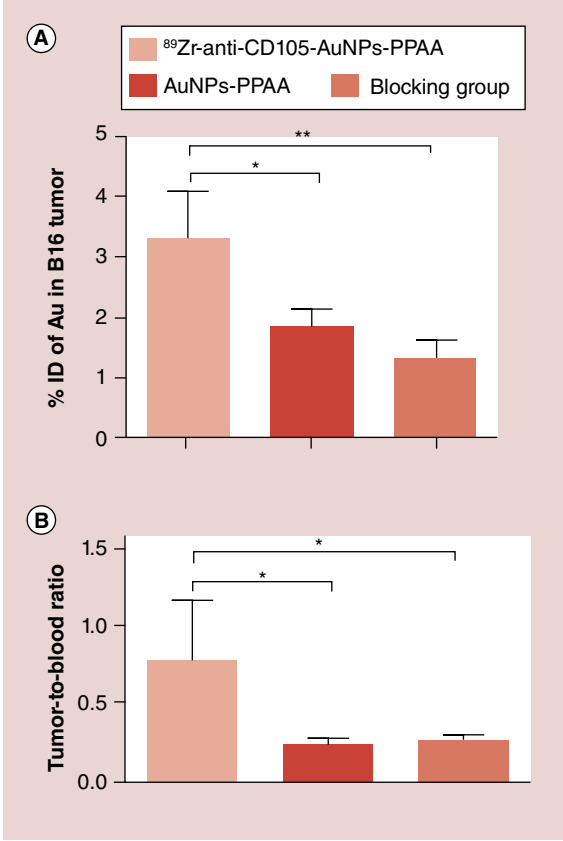

Figure 7. Gold content in (A) tumors and (B) tumor-to-background ratio after intravenous injection of free AuNPs (a total of 36 µg Au per mouse) or anti-CD105-AuNPs-PPAA (a total of 18 µg Au per mouse, corresponding to 100 µg monoclonal antibodies per mouse) or anti-CD105-AuNPs-PPAA (a total of 22 µg Au per mouse, corresponding to a total of 200 µg monoclonal antibodies per mouse) after a blocking dose of anti-CD105 monoclonal antibodies (2 mg monoclonal antibodies per mouse) in B16 melanoma-bearing C57BL/6J mice 6 h after injection. The gold content as measured by ICP-MS is expressed as a percentage of the given dose (%ID). Data are expressed as means ± SD (n = 3–4 animals; 3–4 tumors).
*p < 0.05; **p < 0.01.
Au: Gold; AuNP: Gold nanoparticle.

contrast. Indeed, our previous studies showed that the *in vitro* binding activity of ^{89}Zr-cetuximab-AuNPs-PPAA (EC_{50} value: 0.08 µg ml^{-1}) was reduced by a factor of 2 compared with ^{89}Zr-Df-Bz-NCS-cetuximab (EC_{50} value: 0.19 µg ml^{-1}) [33], while the EC_{50} value of ^{89}Zr-anti-CD105-AuNPs-PPAA was approximately five-times lower than that of ^{89}Zr-Df-Bz-NCS-anti-CD105. The larger size of conjugated anti-CD105 mAbs (100 nm) compared with that of conjugated cetuximab (30 nm) suggests a higher grafting rate of mAb molecules onto the nanoparticle surface (Figure 1) and might explain the observed decrease in tumor targeting (Figure 5A).

Despite the decrease in tumor uptake starting 1 day after injection, the maintained specificity of conjugated anti-CD105 mAbs was confirmed by an *in vivo* saturation experiment, suggesting the selective accumulation of ^{89}Zr-anti-CD105-AuNPs-PPAA in tumors and the preservation of the CD105 recognition property of the antibody after radiolabelling and coupling to AuNPs. In fact, the administration of unlabeled mAbs in excess before ^{89}Zr-anti-CD105-AuNPs-PPAA injection induced the saturation of CD105 binding sites and significantly decreased the CD105 binding of ^{89}Zr-anti-CD105-AuNPs-PPAA in tumors (Figure 6). These results confirmed antigen-specific binding and the partial preservation of antibody immunoreactivity.

On the other hand, ICP-MS analysis quantified the tumor uptake of functionalized AuNPs, functionalized AuNPs after a saturating dose of unlabelled anti-CD105 mAbs (blocking group) and free AuNPs, by determining the Au content at 6 h after injection (Figure 7). The significant decrease of Au content in tumors belonging to the blocking group compared with mice receiving anti-CD105-AuNPs-PPAA without saturating target receptors also confirmed the preservation of antibody specificity after nanoparticle conjugation, since the saturation of CD105 binding sites led to a significant decrease in Au in tumors (Figure 7A). Moreover, the significant higher amount of Au in tumors for mice receiving anti-CD105-AuNPs-PPAA compared with those receiving AuNPs-PPAA highlighted the improved tumor uptake of functionalized nanoparticles. Indeed, the presence of grafted mAbs on the nanoparticle surface might be favorable to directing the nanoimmunoconjugate to the tumor. These ligand–receptor interactions result in improved uptake of the nanocomplex into the tumor. Further studies are needed to assess the interest of active targeting by conjugating nanoparticles to nonspecific antibodies. Moreover, Figure 7B showed the significant higher tumor-to-blood ratio for mice injected with antibody-targeted nanoparticles compared with those receiving free AuNPs. This statement was supported by the significantly lower Au concentration in circulation for mice receiving anti-CD105-AuNPs-PPAA compared with that of mice receiving uncoupled nanoparticles (data not shown). This result is probably related to the greater uptake of anti-CD105-AuNPs-PPAA by the RES, as seen on PET images (Figure 3).

This study highlights the potential of anti-CD105 antibody-labelled AuNPs in tumor detection and demonstrates the preservation of the antibody specificity after nanoparticle conjugation. Regarding cancer therapy, the anticancer effect of anti-CD105 mAbs due to their antiangiogenic properties might be boosted thanks to the photophysical properties of AuNPs. Indeed, previous

studies have shown that AuNPs have interesting anticancer properties through photothermolysis of cancer cells and enhancement of the efficacy of radiotherapy. It must be mentioned that a sufficient amount of Au delivered to tumors is required for these applications. For imaging purposes, as is the case for this study, we injected trace amounts of immunonanoconjugates, which are sufficient for diagnostic applications with a minimal risk of toxicity. However, we should consider increasing the amount of injected conjugates for therapeutic purposes [55–58] and thus assessing the potential toxicity of high amounts of injected AuNPs. Furthermore, photothermal therapy using visible laser is adequate for superficial tumors, such as melanoma, but not for deeper lesions, for which the short-wave radiofrequency field treatment is most suitable [59]. Finally, as it is possible to locally and specifically activate AuNPs accumulated in malignant tissues, the nonspecific uptake of immunonanoconjugates by the RES may be overcome thanks to the local radiation exposure of AuNPs. These encouraging results present new opportunities for nanoparticle-based drug delivery systems in future theranostic applications.

Conclusion & future perspective

Antibody-based targeting of angiogenesis represents a new promising diagnostic and therapeutic tool. Among these tools, anti-CD105 mAbs have shown anticancer benefit in recent clinical studies [60]. Indeed, the proven value of endoglin as the most suitable marker for evaluating tumor angiogenesis [61,62] has led to increasingly focused interest on CD105 as a target for immunoconjugates. On the other hand, AuNPs are the subject of intensive studies in biomedical applications. No studies have investigated the biomedical potential of anti-CD105 mAbs conjugated to AuNPs as immunonanocarriers for vascular targeting detection and therapy of cancer. Moreover, the development of more efficient drug delivery systems is important in effectively targeting cancer. For these reasons, we were interested in AuNPs as scaffolds to which anti-CD105 mAbs are attached as an attractive diagnostic and/or therapeutic tool. These immunonanoconjugates combine the therapeutic properties of anti-CD105 mAbs with those of AuNPs, and might improve antitumor efficacy. In this study, we have demonstrated that, despite decreased tumor uptake after nanoparticle conjugation, the *in vivo* antibody specificity and the tumor contrast in PET imaging are preserved. CD105-dependent tumor targeting was also confirmed by the quantification of Au in tumors. Thus, our studies validate anti-endoglin antibody-functionalized AuNPs as a new tool for diagnostic

Executive summary

Characterization of radioimmunoconjugates and *in vitro* assessment of CD105 targeting

- Anti-CD105 monoclonal antibodies (mAbs) conjugated to gold nanoparticles (AuNPs) were characterized *in vitro* in terms of size, plasmatic stability and binding to the target before *in vivo* experiments.
- The nanoparticle diameters observed by TEM imaging ranged from 3 to 10 nm. The mean diameter of anti-CD105 mAbs after coupling to AuNPs was estimated at approximately 102.6 ± 4.0 nm by differential centrifugal sedimentation.
- The *in vitro* stability in plasma of both radioimmunoconjugates showed that the percentages of dissociation were lower by 10% after 24 h.
- The EC_{50} value was reduced from 1 µg ml^{-1} (for anti-CD105 mAbs) to 5 µg ml^{-1} (for anti-CD105-AuNPs-PPAA). The relative binding affinity remains on the same range (less than 1 log) before and after antibody conjugation to AuNPs.

PET evaluation of ^{89}Zr-labelled anti-CD105 mAbs biodistribution in mice before and after coupling reaction to AuNPs

- The tumor uptake of ^{89}Zr-labelled anti-CD105 mAbs was quantified before and after nanoparticle conjugation using noninvasive PET imaging in mice. The decreased tumor uptake after conjugation reaction is in accordance with the results obtained with an *in vitro* ELISA study. Blocking experiments confirmed the specific tumor targeting of conjugated mAbs.
- The tumor-to-background ratio remained good after the conjugation reaction. The high tumor contrast after nanoparticle conjugation supports the good imaging properties of the radioimmunonanoconjugates.
- The tumor uptake of antibody-targeted AuNPs was also quantified using ICP-MS analysis by determining gold content in tumors, and was compared with the tumor uptake of free nanoparticles. Results highlighted the improved tumor uptake for functionalized nanoparticles. The specificity of anti-CD105 mAbs conjugated to AuNPs was confirmed through ICP-MS by repeating blocking experiments.
- No major accumulation of radioactivity was observed in nonspecific organs, aside from the liver, spleen and lungs, and to a lesser extent bones.
- These results present new opportunities for nanoparticle-based imaging and therapy systems in future theranostic applications.

10.2217/NNM.13.185

and imaging of cancer. The nonspecific RES uptake of immunonanoconjugates could be a limitation in the use of radioactive nanoparticles for systemic metabolic radiotherapy, but not for therapeutic strategies, such as photothermal therapy, where nanoparticle activation can be locally controlled. Overall, ^{89}Zr immuno-PET imaging is a powerful tool for characterizing the *in vivo* properties of such nanocomplex systems and can present new opportunities for drug delivery guided by *in vivo* imaging. These observations lay the groundwork for further theranostic applications and give further credence to the probability of future effective nanoparticle-based therapy systems.

References

Papers of special note have been highlighted as:

- • of interest
- •• of considerable interest

1 Julien DC, Behnke S, Wang G, Murdoch GK, Hill RA. Utilization of monoclonal antibody-targeted nanomaterials in the treatment of cancer. *MAbs* 3(5), 467–478 (2011).

• **Discusses the broad range of nanomaterials, including gold nanoparticles (AuNPs), which are under investigation as potential platforms for the presentation of mAbs either as single or combined therapeutics, and their advantages and limitations in specifically targeting cancer.**

2 Dykman L, Khlebtsov N. Gold nanoparticles in biomedical applications: recent advances and perspectives. *Chem. Soc. Rev.* 41(6), 2256–2282 (2012).

3 Mallidi S, Larson T, Aaron J, Sokolov K, Emelianov S. Molecular specific optoacoustic imaging with plasmonic nanoparticles. *Opt. Express.* 15(11), 6583–6588 (2007).

4 Glaser ES, Massey KL, Zhu C, Curley SA. Pancreatic carcinoma cells are susceptible to noninvasive radio frequency fields after treatment with targeted gold nanoparticles. *Surgery* 148(2), 319–324 (2010).

5 Tiwari PM, Vig K, Dennis VA, Singh R. Functionalized gold nanoparticles and their biomedical applications. *Nanomaterials* 1, 31–63 (2011).

• **Describes recent advances in the field of functionalization of AuNPs and their potential biomedical applications.**

6 Haruta Y, Seon BK. Distinct human leukemia-associated cell surface glycoprotein GP160 defined by monoclonal antibody SN6. *Proc. Natl Acad. Sci. USA* 83(20), 7898–7902 (1986).

7 Westphal JR, Willems HW, Schalkwijk CJ, Ruiter DJ, de Waal RM. A new 180-kDa dermal endothelial cell activation antigen: *in vitro* and *in situ* characteristics. *J. Invest. Dermatol.* 100(1), 27–34 (1993).

8 Burrows FJ, Derbyshire EJ, Tazzari PL *et al.* Up-regulation of endoglin on vascular endothelial cells in human solid tumors: implications for diagnosis and therapy. *Clin. Cancer Res.* 1(12), 1623–1634 (1995).

Financial disclosure

This work was supported by grants from the Walloon Region through the 'TARGAN' project, and from the Belgian National Fund for Scientific Research (FNRS-TELEVIE). The hybridoma (clone MJ7/18) was obtained from the Developmental Studies Hybridoma Bank, developed under the auspices of the NICHD and maintained by The University of Iowa, Department of Biology (IA, USA). The authors have no other relevant affiliations or financial involvement with any organization or entity with a financial interest in or financial conflict with the subject matter or materials discussed in the manuscript apart from those disclosed.

No writing assistance was utilized in the production of this manuscript.

9 Miller DW, Graulich W, Karges B *et al.* Elevated expression of endoglin, a component of the TGF-beta–receptor complex, correlates with proliferation of tumor endothelial cells. *Int. J. Cancer.* 81(4), 568–572 (1999).

10 Fonsatti E, Nicolay HJ, Altomonte M, Covre A, Maio M. Targeting cancer vasculature via endoglin/CD105: a novel antibody-based diagnostic and therapeutic strategy in solid tumours. *Cardiovasc. Res.* 86(1), 12–19 (2010).

11 Wang JM, Kumar S, Pye D, van Agthoven AJ, Krupinski J, Hunter RD. A monoclonal antibody detects heterogeneity in vascular endothelium of tumours and normal tissues. *Int. J. Cancer.* 54(3), 363–370 (1993).

12 Clasper S, Royston D, Baban D *et al.* A novel gene expression profile in lymphatics associated with tumor growth and nodal metastasis. *Cancer Res.* 68(18), 7293–7303 (2008).

13 Yoshitomi H, Kobayashi S, Ohtsuka M *et al.* Specific expression of endoglin (CD105) in endothelial cells of intratumoral blood and lymphatic vessels in pancreatic cancer. *Pancreas* 37(3), 275–281 (2008).

14 Hussein MR. Transforming growth factor-beta and malignant melanoma: molecular mechanisms. *J. Cutan. Pathol.* 32(6), 389–395 (2005).

15 Sun T, Sun BC, Ni CS *et al.* Pilot study on the interaction between B16 melanoma cell-line and bone-marrow derived mesenchymal stem cells. *Cancer Lett.* 263(1), 35–43 (2008).

16 Letamendía A, Lastres P, Almendro N *et al.* Endoglin, a component of the TGF-beta receptor system, is a differentiation marker of human choriocarcinoma cells. *Int. J. Cancer* 76(4), 541–546 (1998).

17 Kumar S, Ghellal A, Li C *et al.* Breast carcinoma: vascular density determined using CD105 antibody correlates with tumor prognosis. *Cancer Res.* 59(4), 856–861 (1999).

18 Romani AA, Borghetti AF, Del Rio P, Sianesi M, Soliani P. The risk of developing metastatic disease in colorectal cancer is related to CD105-positive vessel count. *J. Surg. Oncol.* 93(6), 446–455 (2006).

19 Marioni G, D'Alessandro E, Giacomelli L, Staffieri A. CD105 is a marker of tumour vasculature and a potential target for the treatment of head and neck squamous cell carcinoma. *J. Oral Pathol. Med.* 39(5), 361–367 (2010).

20 Tanaka F, Otake Y, Yanagihara K *et al.* Evaluation of angiogenesis in non-small cell lung cancer: comparison between anti-CD34 antibody and anti-CD105 antibody. *Clin. Cancer Res.* 7(11), 3410–3415 (2001).

21 Li C, Gardy R, Seon BK *et al.* Both high intratumoral microvessel density determined using CD105 antibody and elevated plasma levels of CD105 in colorectal cancer patients correlate with poor prognosis. *Br. J. Cancer* 88(9), 1424–1431 (2003).

22 Charpin C, Dales JP, Garcia S *et al.* Tumor neoangiogenesis by CD31 and CD105 expression evaluation in breast carcinoma tissue microarrays. *Clin. Cancer Res.* 10(17), 5815–5819 (2004).

23 Carmeliet P, Jain RK. Molecular mechanisms and clinical applications of angiogenesis. *Nature* 473(7347), 298–307 (2011).

24 Mitchell DC, Bryan BA. Anti-angiogenic therapy: adapting strategies to overcome resistant tumors. *J. Cell. Biochem.* 111(3), 543–553 (2010).

25 Gasparini G, Longo R, Fanelli M, Teicher BA. Combination of antiangiogenic therapy with other anticancer therapies: results, challenges, and open questions. *J. Clin. Oncol.* 23(6), 1295–1311 (2005).

26 Seon BK, Matsuno F, Haruta Y, Kondo M, Barcos M. Long-lasting complete inhibition of human solid tumors in SCID mice by targeting endothelial cells of tumor vasculature with anti-human endoglin immunotoxin. *Clin. Cancer Res.* 3(7), 1031–1044 (1997).

27 Matsuno F, Haruta Y, Kondo M, Tsai H, Barcos M, Seon BK. Induction of lasting complete regression of preformed distinct solid tumors by targeting the tumor vasculature using two new anti-endoglin monoclonal antibodies. *Clin. Cancer Res.* 5(2), 371–382 (1999).

28 Tabata M, Kondo M, Haruta Y, Seon BK. Antiangiogenic radioimmunotherapy of human solid tumors in SCID mice using ^{125}I-labeled anti-endoglin monoclonal antibodies. *Int. J. Cancer* 82(5), 737–742 (1999).

29 Takahashi N, Haba A. Matsuno F, Seon BK. Antiangiogenic therapy of established tumors in human skin/severe combined immunodeficiency mouse chimeras by anti-endoglin (CD105) monoclonal antibodies, and synergy between anti-endoglin antibody and cyclophosphamide. *Cancer Res.* 61(21), 846–854 (2001).

30 Tsujie M, Uneda S, Tsai H, Seon BK. Effective anti-angiogenic therapy of established tumors in mice by naked anti-human endoglin (CD105) antibody: differences in growth rate and therapeutic response between tumors growing at different sites. *Int. J. Oncol.* 29(5), 1087–1094 (2006).

31 Tsujie M, Tsujie T, Toi H *et al.* Anti-tumor activity of an anti-endoglin monoclonal antibody is enhanced in immunocompetent mice. *Int. J. Cancer* 122(10), 2266–2273 (2008).

32 Uneda S, Toi H, Tsujie T *et al.* Anti-endoglin monoclonal antibodies are effective for suppressing metastasis and the primary tumors by targeting tumor vasculature. *Int. J. Cancer* 125(6), 1446–1453 (2009).

33 Marega R, Karmani L, Flamant L *et al.* Antibody-functionalized polymer-coated gold nanoparticles targeting cancer cells: an *in vivo* and *in vitro* study. *J. Mater. Chem.* 22(39), 21305–21312 (2012).

•• **Describes the characterization of AuNPs and cetuximab conjugated to AuNPs before *in vivo* experiments, and assesses the biodistribution of iodinated cetuximab before and after nanoparticle conjugation by *ex vivo* studies.**

34 Karmani L, Labar D, Valembois V *et al.* Antibody-functionalized nanoparticles for imaging cancer: influence of conjugation to gold nanoparticles on the biodistribution of ^{89}Zr-labeled cetuximab in mice. *Contrast Media Mol. Imaging* 8(5), 402–408 (2013).

•• **Compares the biodistribution pattern of cetuximab-targeted AuNPs and unconjugated cetuximab in mice using noninvasive ^{89}Zr immuno-PET studies.**

35 Vugts DJ, van Dongen GAMS. ^{89}Zr-labeled compounds for PET imaging guided personalized therapy. *Drug Discov. Today Technol.* 8(2–4), e53–e61 (2011).

36 van Dongen GAMS, Visser GWM, Lub-de-Hooge MN, De Vries EG, Perk LR. Immuno-PET: a navigator in monoclonal antibody development and applications. *Oncologist* 12(12), 1379–1389 (2007).

37 Holland JP, Sheh YC, Lewis JS. Standardized methods for the production of high specific-activity zirconium-89. *Nucl. Med. Biol.* 36(7), 729–739 (2009).

38 Kandil SA, Scholten B, Saleh ZA, Youssef AM, Qaim SM, Coenen HH. A comparative study on the separation of radiozirconium via ion-exchange and solvent extraction techniques, with particular reference to the production of ^{88}Zr and ^{89}Zr in proton induced reactions on yttrium. *J. Radioanal. Nucl. Chem.* 274(1), 45–52 (2007).

39 Vosjan MJWD, Perk LR, Visser GW *et al.* Conjugation and radiolabeling of monoclonal antibodies with zirconium-89 for PET imaging using the bifunctional chelate p-isothiocyanatobenzyl-desferrioxamine. *Nat. Prot.* 5(4), 739–743 (2010).

40 Perk LR, Vosjan MJWD, Visser GW *et al.* p-Isothiocyanatobenzyl-desferrioxamine: a new bifunctional chelate for facile radiolabeling of monoclonal antibodies with zirconium-89 for immuno-PET imaging. *Eur. J. Nucl. Med. Mol. Imaging* 37(2), 250–259 (2010).

41 Moreau N, Michiels C, Masereel B *et al.* PVD synthesis and transfer into water-based solutions of functionalized gold nanoparticles. *Plasma Process Polymer.* 6(1), S888–S892 (2009).

• **Describes the synthesis and coating of AuNPs by PVD techniques, and highlights the crucial role of coating to prevent AuNP aggregation when transferred into liquid solutions, which facilitates their functionalization for future studies.**

42 Masereel B, Dinguizli M, Bouzin C *et al.* Antibody immobilization on gold nanoparticles coated layer-by-layer with polyelectrolytes. *J. Nanopart. Res.* 13(4), 1573–1580 (2011).

10.2217/NNM.13.185

43 Hong H, Yang Y, Zhang Y *et al.* Positron emission tomography imaging of CD105 expression during tumor angiogenesis. *Eur. J. Nucl. Med. Mol. Imaging.* 38(7), 1335–1343 (2011).

44 Huisman MC, Reder S, Weber AW, Ziegler SI, Schwaiger M. Performance evaluation of the Philips MOSAIC small animal PET scanner. *Eur. J. Nucl. Med. Mol. Imaging* 34(4), 532–540 (2007).

45 Alkilany AM, Murphy CJ. Toxicity and cellular uptake of gold nanoparticles: what we have learned so far? *J. Nanopart. Res.* 12(7), 2313–2333 (2010).

46 Garnett MC, Kallinteri P. Nanomedicines and nanotoxicology: some physiological principles. *Occup. Med. (Lond.)* 56(5), 307–311 (2006).

47 Hirota K, Hasegawa T, Hinata H *et al.* Optimum conditions for efficient phagocytosis of rifampicin-loaded PLGA microspheres by alveolar macrophages. *J. Control. Release* 119(1), 69–76 (2007).

48 Videira MA, Botelho MF, Santos AC, Gouveia LF, de Lima JJ, Almeida AJ. Lymphatic uptake of pulmonary delivered radiolabelled solid lipid nanoparticles. *J. Drug Target.* 10(8), 607–613 (2002).

49 He C, Hu Y, Yin L, Tang C, Yin C. Effects of particle size and surface charge on cellular uptake and biodistribution of polymeric nanoparticles. *Biomaterials* 31(13), 3657–3666 (2010).

50 Mahmoud M, Borthwick GM, Hislop AA, Arthur HM. Endoglin and activin receptor-like-kinase 1 are co-expressed in the distal vessels of the lung: implications for two familial vascular dysplasias, HHT and PAH. *Lab. Invest.* 89(1), 15–25 (2009).

51 De Jong WH, Hagens WI, Krystek P, Burger MC, Sips AJ, Geertsma RE. Particle size-dependent organ distribution of gold nanoparticles after intravenous administration. *Biomaterials* 29(12), 1912–1919 (2008).

52 Tinianow JN, Gill HS, Ogasawara A *et al.* Site-specifically ^{89}Zr-labeled monoclonal antibodies for ImmunoPET. *Nucl. Med. Biol.* 37(3), 289–297 (2010).

53 Mealey J Jr. Turn-over of carrier-free zirconium-89 in man. *Nature* 179(4561), 673–674 (1957).

54 Abou DS, Ku T, Smith-Jones PM. *In vivo* biodistribution and accumulation of ^{89}Zr in mice. *Nucl. Med. Biol.* 38(5), 675–681 (2011).

55 Glazer ES, Curley SA. Radiofrequency field-induced thermal cytotoxicity in cancer cells treated with fluorescent nanoparticles. *Cancer* 116(13), 3285–3293 (2010).

56 Moran CH, Wainerdi SM, Cherukuri TK *et al.* Size-dependent joule heating of gold nanoparticles using capacitively coupled radiofrequency fields. *Nano Res.* 2(5), 400–405 (2009).

57 Chang MY, Shiau AL, Chen YH, Chang CJ, Chen HH, Wu CL. Increased apoptotic potential and dose-enhancing effect of gold nanoparticles in combination with single-dose clinical electron beams on tumor-bearing mice. *Cancer Sci.* 99(7), 1479–1484 (2008).

58 Hainfeld JF, Slatkin DN, Smilowitz HM. The use of gold nanoparticles to enhance radiotherapy in mice. *Phys. Med. Biol.* 49(18), N309–N315 (2004).

59 Raoof M, Curley SA. Non-invasive radiofrequency-induced targeted hyperthermia for the treatment of hepatocellular carcinoma. *Int. J. Hepatol.* 676957 (2011).

60 Rosen LS, Hurwitz HI, Wong MK *et al.* A Phase I first-in-human study of TRC105 (anti-endoglin antibody) in patients with advanced cancer. *Clin. Cancer Res.* 18(17), 4820–4829 (2012).

•• **Reports the first-in-human Phase I study using anti-endoglin antibody (TRC105) in order to investigate its safety, pharmacokinetics and antitumor activity in patients with advanced refractory solid tumors.**

61 Fonsatti E, Del Vecchio L, Altomonte M *et al.* Endoglin: an accessory component of the TGF-beta-binding receptor-complex with diagnostic, prognostic, and bioimmunotherapeutic potential in human malignancies. *J. Cell. Physiol.* 188(1), 1–7 (2001).

62 Wang JM, Kumar S, Pye D, van Agthoven AJ, Krupinski J, Hunter RD. A monoclonal antibody detects heterogeneity in vascular endothelium of tumours and normal tissues. *Int. J. Cancer* 54(3), 363–370 (1993).

Affiliations

Linda Karmani
Biomedical Magnetic Resonance Group (REMA), Louvain Drug Research Institute, Université Catholique de Louvain, Avenue Mounier 73, 1200 Brussels, Belgium

Virginie Bouchat
Research Centre for the Physics of Matter and Radiation (PMR-LARN), Namur Research Institute for Life Sciences (NARILIS), University of Namur, Rue de Bruxelles 61, 5000 Namur, Belgium

Caroline Bouzin
Pharmacology and Therapeutics Unit (FATH), Institute of Experimental and Clinical Research (IREC), Université Catholique de Louvain, Avenue Mounier 53, 1200 Brussels, Belgium

Philippe Levêque
Biomedical Magnetic Resonance Group (REMA), Louvain Drug Research Institute, Université Catholique de Louvain, Avenue Mounier 73, 1200 Brussels, Belgium

Daniel Labar
Centre for Molecular Imaging, Radiotherapy and Oncology (MIRO), Institute of Experimental and Clinical Research (IREC), Université Catholique de Louvain, Avenue Hippocrate 54, 1200 Brussels, Belgium

Anne Bol
Centre for Molecular Imaging, Radiotherapy and Oncology (MIRO), Institute of Experimental and Clinical Research (IREC), Université Catholique de Louvain, Avenue Hippocrate 54, 1200 Brussels, Belgium
Gladys Deumer
Laboratory of Analytical Biochemistry and Louvain Centre for Toxicology and Applied Pharmacology (LTAP), Avenue Hippocrate 10, 1200 Brussels, Belgium
Riccardo Marega
Department of Chemistry and Namur Research College (NARC), University of Namur, Rue de Bruxelles 61, 5000 Namur, Belgium
Davide Bonifazi
Department of Chemistry and Namur Research College (NARC), University of Namur, Rue de Bruxelles 61, 5000 Namur, Belgium
Vincent Haufroid
Laboratory of Analytical Biochemistry and Louvain Centre for Toxicology and Applied Pharmacology (LTAP), Avenue Hippocrate 10, 1200 Brussels, Belgium
Carine Michiels
Unité de Recherche en Biologie Cellulaire (URBC), Namur Research Institute for Life Sciences (NARILIS), University of Namur, Rue de Bruxelles 61, 5000 Namur, Belgium
Vincent Grégoire
Centre for Molecular Imaging, Radiotherapy and Oncology (MIRO), Institute of Experimental and Clinical Research (IREC), Université Catholique de Louvain, Avenue Hippocrate 54, 1200 Brussels, Belgium
Olivier Feron
Pharmacology and Therapeutics Unit (FATH), Institute of Experimental and Clinical Research (IREC), Université Catholique de Louvain, Avenue Mounier 53, 1200 Brussels, Belgium
Stéphane Lucas
Research Centre for the Physics of Matter and Radiation (PMR-LARN), Namur Research Institute for Life Sciences (NARILIS), University of Namur, Rue de Bruxelles 61, 5000 Namur, Belgium
Thierry Vander Borght
Centre for Molecular Imaging, Radiotherapy and Oncology (MIRO), Institute of Experimental and Clinical Research (IREC), Université Catholique de Louvain, Avenue Hippocrate 54, 1200 Brussels, Belgium
Bernard Gallez
Biomedical Magnetic Resonance Group (REMA), Louvain Drug Research Institute, Université Catholique de Louvain, Avenue Mounier 73, 1200 Brussels, Belgium

10.2217/NNM.13.185